Material Ductility and Toughening Mechanism of Polypropylene Blended with Bimodal Distributed Particle Size of Styrene–Ethylene–Butadiene–Styrene Triblock Copolymer at High Strain Rate

Hiroyuki Mae,[1] Masaki Omiya,[2] Kikuo Kishimoto[3]

[1]*Honda R&D Co., Ltd., 4630 Shimotakanezawa, Haga-machi, Haga-gun, Tochigi 321-3393, Japan*
[2]*Department of Mechanical Engineering, Keio University, 3-14-1, Hiyoshi, Kohoku-ku, Yokohama-shi, Kanagawa, 223-8522 Japan*
[3]*Department of Mechanical and Sciences Engineering, Tokyo Institute of Technology, 2-12-1, O-okayama, Meguro, Tokyo 152-8552, Japan*

Received 6 February 2008; accepted 29 June 2008
DOI 10.1002/app.28959
Published online 19 September 2008 in Wiley InterScience (www.interscience.wiley.com).

ABSTRACT: The material ductility and toughening mechanisms under high strain rate are characterized in the polypropylene (PP) blended with two different styrene–ethylene–butadiene–styrene triblock copolymer (SEBS) by the tensile tests at the nominal strain rates from 0.3 to 100 s^{-1}, fracture surface observations, interparticle distances, and the morphological finite element (FE) analyses. It is found that the bimodal-distributed SEBS particle morphology enhances the impact material ductility by craze bands formation, which is caused by the stress interaction between large rubber particles with the highly elongated small rubber particles inside the fibrils of the craze. It is found that there are three conditions for craze bands formation. The first condition is that the total SEBS content is larger than 15 wt %. Second condition is that the weight ratio of small SEBS particles against total SEBS particles should be larger than 0.06. Third condition is that the interparticle distance of large SEBS particles should be larger than 100 nm. In the numerical aspects, the present constitutive law with the craze nucleation and growth can successfully predict the craze bands in the microstructural FE models, leading to the useful procedure for identifying the ductile brittle transition based on the microstructure. The synergistic effect of these rubber particles gives rise to a strong increase in the ductility of these bimodal rubber particle distributed PP systems. © 2008 Wiley Periodicals, Inc. J Appl Polym Sci 110: 3941–3953, 2008

Key words: mechanical properties; particle size distribution; crazing; poly(propylene) (PP); TEM

INTRODUCTION

Polypropylene (PP) has been extensively used for many applications such as interior and exterior automobile components especially in the automobile applications.[1] Lately, syntactic PP foams are being used to replace the traditional PP bulk components for weight reduction.[2,3] It is well known that the impact resistance of polymeric materials can be considerably modified by the incorporation of rubber materials.[4–12] Mechanical properties of their blends are controlled by their morphology to a great extent. For rubber toughened polymers the shape, content, size, and size distribution of the dispersed-phase particles have major effects on mechanical properties of polymer–elastomer blends.[12–28]

The bimodal rubber particle size distribution is another approach for the improvement of rubber toughening in polymers.[29–33] Recently, PP toughened with styrene–ethylene–butadiene–styrene triblock copolymer (SEBS) has been extensively used for interior or exterior of the automotive parts. However, the study of PP toughened with a bimodal distribution of SEBS particles is quite few. In addition, the effect of strain rate on the tensile mechanical properties has not been extensively reported in PP toughened with a bimodal size distributed SEBS particles. Then, our previous study clarified the toughening mechanism for PP toughened with the bimodal rubber particle size distribution whose total rubber content was 30 wt % by describing the effect of the bimodal distribution of SEBS particle size on the tensile mechanical properties such as elastic modulus, yield stress, and rupture strain at nominal strain rates from 0.3 to 100 s^{-1}.[34] On the basis of the results of our previous study, the important parameters are the interparticle distance between large SEBS particles and the location of small SEBS particles for

Correspondence to: H. Mae (Hiroyuki_Mae@n.t.rd.honda.co.jp).

TABLE I
Detail of SEBS

Name	MFR (g/10 min at 230°C)	Weight ratio of stylene/ethylene–butylene (%)
H1221 (SEBS A)	4.5	12/88
H1062 (SEBS B)	4.5	18/82

increasing the material ductility. Then, the effect of total rubber contents was further studied by the same authors by changing the blend ratio of total rubber content as 10, 20, and 30 wt %.[35] However, our previous study focused on the material system where the total SEBS contents were only three levels such as 10, 20, and 30 wt % against PP matrix. It is important to investigate more preciously, the effect of the total rubber content on the toughening mechanisms of bimodal rubber particle size distributed PP blends for further understanding. In addition, it is very interesting to understand the effect of total rubber content on the material ductility in the bimodal rubber particle size distributed PP blend system because the important parameters such as the interparticle distance between large particles and the location of small particles depend strongly on the total content of rubber blend.

In this study, PP and two types of SEBS were blended so that the total rubber contents were 10, 15, 20, 25, and 30 wt % against PP by the same blending procedure as our previous study. The morphology of polymer blends was observed, and the distribution sizes of the SEBS particles were analyzed by transmission electron microscopy (TEM). Tensile tests were conducted at nominal strain rates from 0.3 to 100 s^{-1}. The fracture surfaces were observed by scanning electron microscopy (SEM) to understand the difference of the toughening mechanism for PP toughened with the bimodal rubber particle size distribution in PP and SEBS blends. In addition, the finite element (FE) analyses were carried out by developing the plane strain microstructural FE models based on the morphological pictures to investigate stress distributions and craze evolutions around SEBS particles.

EXPERIMENTAL

Materials

Isotactic polypropylene (i-PP: J-3003GV, Prime Polymer, Japan) whose molecular weight M_n was about 33,000 was used as the matrix polymer in this study. It has a melt flow rate = 30 g/10 min (230°C). The density of i-PP was 900 kg/m^3. Two types of SEBS [H1221 (SEBS A) and H1062 (SEBS B), Asahi Kasei Chemicals, Japan] were used as shown in Table I. The nominal diameter of SEBS A was 80 nm and SEBS B was 250 nm. The density of SEBS A and SEBS B was 890 kg/m^3. Thus, it is considered that the volume fraction was almost same as the weight fraction in all the blends in this study.

Blending and sample preparation

PP and SEBS copolymers were melt mixed in a corotating twin screw extruder (Berstorff, ZE40A), with a screw diameter of 40 mm. The temperature profile was controlled at 180, 180, 190, and 192°C from feed to die zones. The screw speed was kept constant at 200 rpm. To blend two types of SEBS in PP matrix, SEBS B and PP were melt mixed, firstly. After that, SEBS A and PP + SEBS B were melt mixed at the same condition as the case of SEBS B and PP. The blend ratio between SEBS A and SEBS B in the total rubber content of 10 wt % were 0/10, 2.5/7.5, 5/5, 7.5/2.5, and 10/0 wt %, respectively. In the total rubber content of 15 wt %, the blend ratio between SEBS A and B were 0/15, 3.75/11.25, 7.5/7.5, 11.25/3.75, and 15/0 wt %, respectively. The blend ratio between SEBS A and SEBS B in the total rubber content of 20 wt % were 0/20, 5/15, 10/10, 15/5, and 20/0 wt %, respectively. In the total rubber content of 25 wt %, the blend ratio between SEBS A and B were 0/25, 6.25/18.75, 12.5/12.5, 18.75/6.25, and 25/0 wt %, respectively. In the total rubber content of 30 wt %, the blend ratio between SEBS A and B were 0/30, 7.5/22.5, 15/15, 22.5/7.5, and 30/0 wt %, respectively. Thus, our present study focuses on totally 10, 15, 20, 25, and 30 wt % rubber blended PP for understanding the effect of total rubber content on the material ductility in the bimodal particle size distributed blends. Then, the hot extrudate was immediately quenched in a water bath and palletized. All blends were prepared under the same conditions as the previous study.[34,35] The blends were injection molded to the rectangular plate whose geometry was 150 mm × 150 mm × 3 mm. The temperature profile from the barrel to die was 200, 200, 190, and 180°C, and the mold temperature was 45°C. Finally, all tensile test specimens were cut out of the plates in such that the tensile direction was same as the injection direction.

Tensile test

ASTM dumbbell-shaped (parallel portion width 4.8 mm) micro tensile test specimens are used for measuring the stress–strain relationship (ASTM D1708). Figure 1 shows the shape of the test specimen. The thickness of test specimen is 3 mm. This study uses a servo-hydraulic high-speed impact test apparatus (Shimazu EHF U2H-20L: maximum tensile speed 15 m/s) to obtain mechanical characteristics under

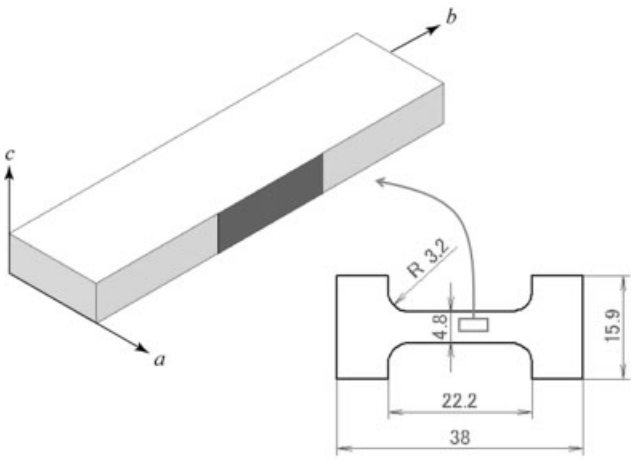

Figure 1 ASTM tensile test specimen and cutting location of thin specimen.

medium to high speed deformation. The nominal strain and nominal strain rate were calculated from the clamping distance of the test specimen where the gauge length was 22.2 mm. The nominal strain rate ranges from 0.3 to 100 s^{-1}. Fracture surface was observed by scanning electron microscopy (SEM: HITACHI *S*-4300SE/N).

Morphological investigation

Transmission electron microscope (TEM: JEOL JEM-200CX) operating at 100 keV was used to observe the phase morphology. After staining of samples with OsO_4, ultrathin sections were sliced by ultra microtome equipped with diamond knife. In this study, two blends (SEBS A/SEBS B = 5/5 and 10/10 wt %) were observed by TEM. In our previous study, three blends (SEBS A/SEBS B = 7.5/22.5, 15/15, and 22.5/7.5 wt %) were observed by TEM.[34,35] The obtained results showed that the two-step blending procedure worked well for making the bimodal particle size distribution in PP/SEBS A/SEBS B blends. In addition, it was shown that the interparticle distances of large SEBS particles (ID_{large}) based on image analyses were similar to those estimated by the equation proposed by Wu.[36] Thus, the particle size distribution and the interparticle distance were validated in only two blends (SEBS A/SEBS B = 5/5 and 10/10 wt %) in this study. Figure 2(a–c) shows the morphology of the representative PP/SEBS A/SEBS B blends, where a two-phase morphology is clearly seen. Figure 2(a) is the morphology of the blends (PP/SEBS A/SEBS B = 90/5/5 wt %), whereas Figure 2(b) is that of the blend (PP/SEBS A/SEBS B = 80/10/10 wt %). Figure 2(c) shows the morphology of the blend (PP/SEBS A/SEBS B = 70/15/15 wt %) from the previous study.[34,35] The large particle SEBS domains are elongated and ellipsoid due to the injection molding process although SEBS particles are dispersed randomly in the PP matrix. The shape of these domains would influence the stress concentration near the rubber particles. However, the loading direction in this study was parallel to the elongated direction of these domains, and the stress concentration would be smaller than the sphere shape domain. Under this situation, it is considered that the distance between large particles is most important parameter for toughening because this distance indicates the stress overlapping between rubber particles and the degree of craze formation in matrix materials. Figure 3(a–c) shows the histograms of the rubber particle sizes measured by image analyses. In the image analysis, the commercial based software (Azo-kun, Asahi Kasei Engineering, Japan) was used. As shown in Figure 2, the SEBS particles shapes were ellipsoid. It was assumed that the SEBS particles shapes were sphere, and the diameters were the average diameters of the long and short diameters of ellipsoidal particles. The diameter of each circle was collected manually in the software because they could not be identified by the threshold of the black–white images. As shown clearly, all three compositions show a bimodal distribution of the rubber particle sizes. In the blend (PP/SEBS A/SEBS B = 90/5/5), the first peak of the particle diameter ranges approximately from 80 to 200 nm, whereas the second peak of the particle diameter ranges from 220 to 280 nm. In the blend (PP/SEBS A/SEBS B = 80/10/10), the first particle size distribution ranges from 100 to 180 nm, whereas the second one ranges from 220 to 280 nm approximately. In the blend (PP/SEBS A/SEBS B = 70/15/15), the particle size distributions firstly ranges from about 80 to 140 nm. The second particle distribution ranges from 200 to 250 nm. It is considered that the blending procedure, where each SEBS was melt mixed with PP respectively, would work well because the particles were distributed randomly in the PP matrix. Further investigation about the mixing procedure such as another blending procedure, where PP and SEBS A are mixed first and then PP+SEBS A and SEBS B are mixed will be the future work.

Numerical procedure

To investigate stress distributions, craze nucleation, and growth around SEBS particles, FE analyses were carried out by developing the plane strain microstructural model based on the morphological TEM pictures. Figure 4 shows the microstructural FE models developed by using OOF software[37] with the boundary conditions in the blends of 90/5/5, 80/10/10, and 70/15/15. The left-hand side was constrained for their horizontal movements, and the

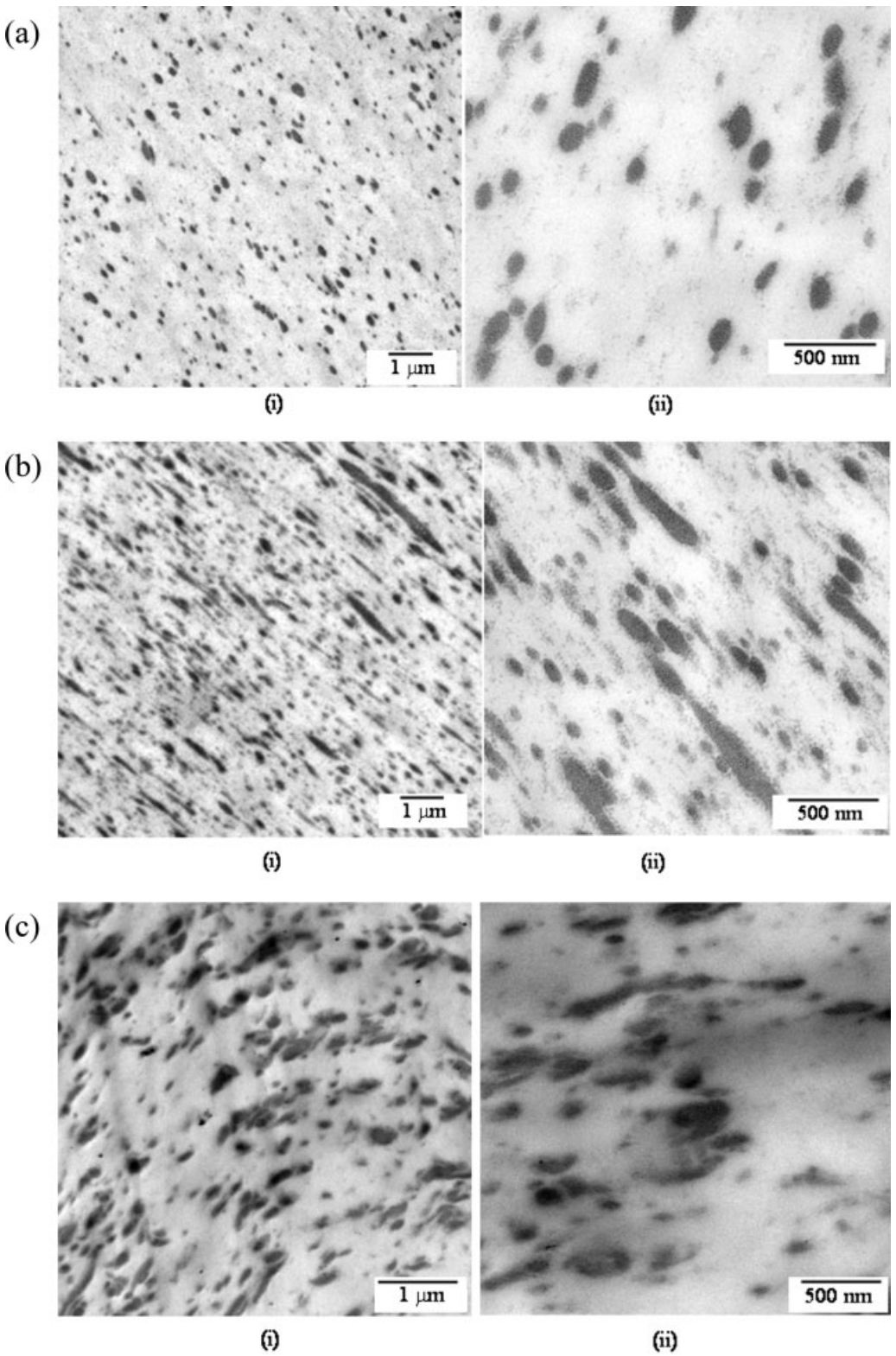

Figure 2 (a) Morphology of blend (PP/SEBS A/SEBS B = 90/5/5). (b) Morphology of blend (PP/SEBS A/SEBS B = 80/10/10). (c) Morphology of blend (PP/SEBS A/SEBS B = 70/15/15).

bottom side was fixed for its vertical movement. The enforced displacement was applied on the right-hand side and the upper side. The applied strain rate corresponded to 100 s^{-1} in both directions. The FE analyses were carried out by using the general explicit solver, RADIOSS version 4.4 with the user defined material subroutine program developed for predicting the craze nucleation and growth.[38–41]

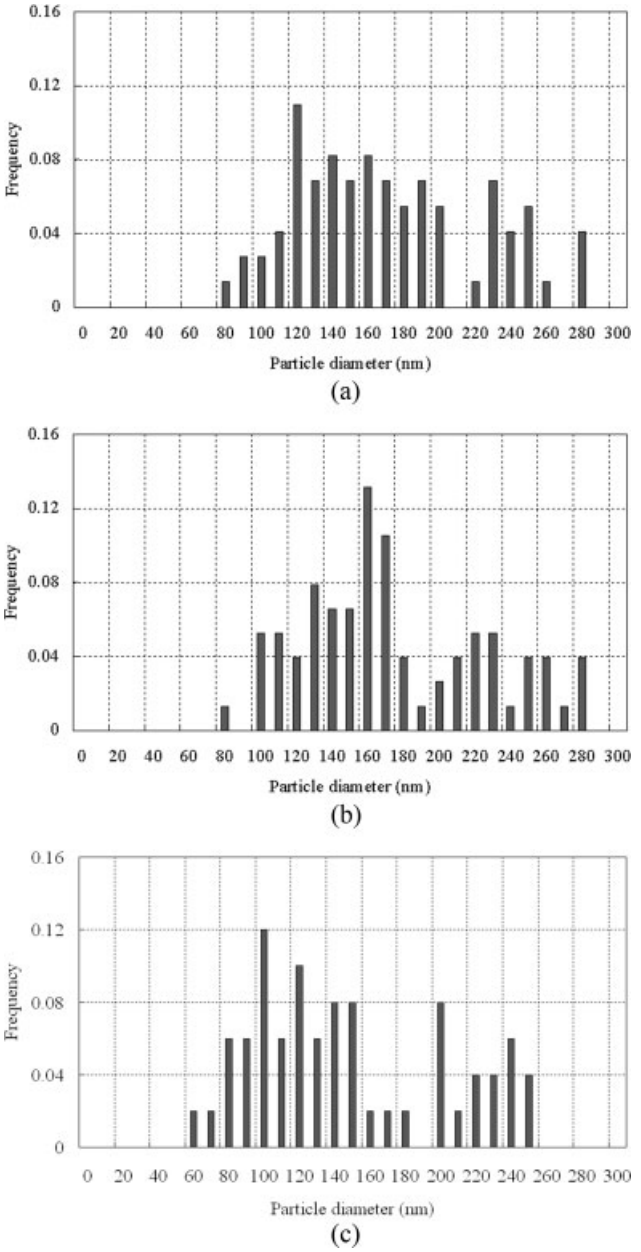

Figure 3 (a) Histogram of particle diameter of blend (PP/SEBS A/SEBS B = 90/5/5). (b) Histogram of particle diameter of blend (PP/SEBS A/SEBS B = 80/10/10). (c) Histogram of particle diameter of blend (PP/SEBS A/SEBS B = 70/15/15).

The proposed elastoviscoplastic constitutive equation with craze effect is shown as eq. (1):[38,39]

$$\overset{\nabla}{\mathbf{T}} = \mathbf{C}^v : \mathbf{D} - \dot{\bar{\varepsilon}}^{\mathrm{p}}(\cos\delta)\mathbf{P}' - \dot{\omega}\mathbf{T}/(1-\omega), \qquad (1)$$

where $\mathbf{T}$ is Cauchy stress, $\mathbf{D}$ is deformation rate, $\dot{\bar{\varepsilon}}^p$ is equivalent plastic strain rate, ω is craze density, $\dot{\omega}$ is craze density rate and $(\overset{\nabla}{})$ is Jaumann rate. $\mathbf{C}^v$, $\mathbf{P}'$, and $\cos\delta$ are defined in the following equations:

$$\mathbf{C}^v \equiv H_\omega(1-\omega)/(H_\omega + 3\mu) \times \left[\mathbf{C}^{\mathrm{e}} + 3\mu/H \times \left\{(3\lambda+2\mu)/3\mathbf{I}\otimes\mathbf{I} + 3\mu\mathbf{T}'\otimes\mathbf{T}'/\bar{\sigma}^2\right\}\right], \qquad (2)$$

$$\mathbf{P}' \equiv \mathbf{C}^v : \mathbf{m}' = 3\mu(1-\omega)\mathbf{T}'/\bar{\sigma}, \quad \mathbf{m}' \equiv 3/2\mathbf{T}'/\bar{\sigma}, \qquad (3)$$

$$H_\omega \equiv /(1-\omega)\bar{\sigma}/(\dot{\bar{\varepsilon}}^{\mathrm{p}}k), \quad \bar{\sigma} \equiv (3\overset{\nabla}{\mathbf{T}}'\overset{\nabla}{\mathbf{T}}'/2)^{1/2}, \qquad (4)$$

$$\cos\delta = \left(1-\sin^2\delta\right)^{1/2}, \quad \sin\delta = k(m)\sin\alpha, \qquad (5)$$

where $\mathbf{m}'$ is stress direction tensor, m is the strain rate sensitivity parameter, and $\cos\alpha$ is defined as

$$\cos\alpha \equiv \mathbf{T}'\cdot\overset{\nabla}{\mathbf{T}}'(\mathbf{T}'\cdot\mathbf{T}')^{-1/2}(\overset{\nabla}{\mathbf{T}}'\cdot\overset{\nabla}{\mathbf{T}}')^{-1/2}. \qquad (6)$$

The craze evolution equation is proposed in the following equation[40]:

$$\dot{\omega} = A(1-\omega)\langle\dot{\varepsilon}^{\mathrm{p}}_m\rangle + 1/2BD_1^{\dot{\bar{\varepsilon}}^{\mathrm{p}}} \times [1+\tanh\{-D_2(\bar{\varepsilon}^{\mathrm{p}}-\varepsilon_c)\}]\dot{\bar{\varepsilon}}^{\mathrm{p}}, \qquad (7)$$

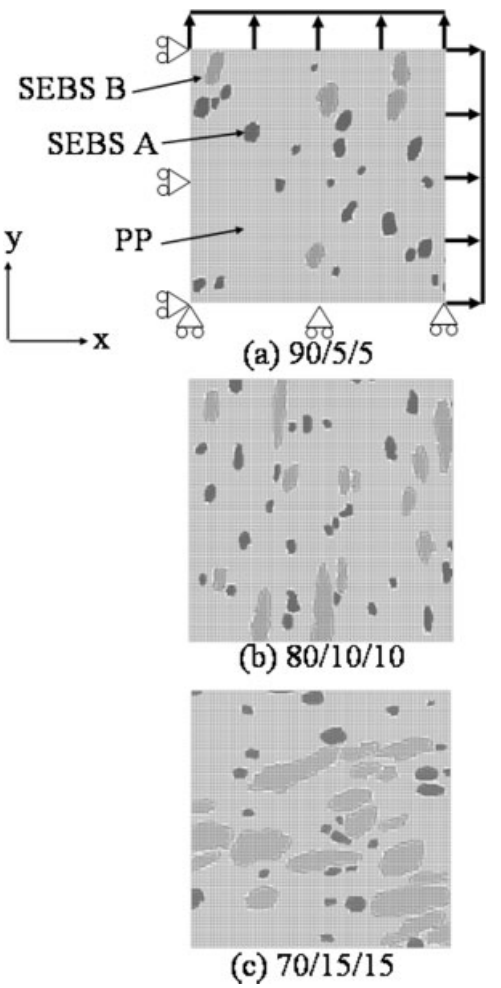

Figure 4 Finite element models for three blends.

TABLE II
Material Constants for Finite Element Analysis

A	0.383
B	1.226
A_1	1.982 (MPa)
B_1	417.665 (MPa)
D_1	0.999
D_2	100.541
ε_c	1.087
m	0.069
$\dot{\varepsilon}_r$	1 (s^{-1})
σ_r	10.055 (MPa)
σ_y	17.432 (MPa)
k_1	44.795
k_2	0.863
k_3	1.243
q_1	0.0001177
q_2	12.44
q_3	2.908
ε_r	0.0001

where A, B, D_1, and D_2 are material constants. $\dot{\varepsilon}_m^{\mathrm{p}}$ is the mean normal plastic strain rate defined as

$$\dot{\varepsilon}_m^p = \left\{(q_1\omega)\cosh\left((q_2\omega + q_3)\sigma_m/\sigma_y\right)\right\}^{\bullet}, \quad (8)$$

where σ_m is the hydrostatic stress, σ_y is the yield stress, q_1–q_3 are material constants. The first part of eq. (7) means craze evolution, and the second one means the craze creation and growth. ε_c is the strain at which the craze stops growing. The craze generation is based on the hydrostatic stress criterion as shown in eq. (9).

$$\sigma_b \geq A_1 + (B_1/3\sigma_m) \quad \sigma_b = \sigma_1 - v\sigma_2 - v\sigma_3, \quad (9)$$

in which σ_b is the stress needed for fibril orientation, σ_m is the hydrostatic stress, $\sigma_1 - \sigma_3$ are the principal stresses, A_1 and B_1 are material constants.

With strain rate-dependent coefficient m, the strain hardening equation is modeled in the following equations:

$$\dot{\bar{\varepsilon}}^{\mathrm{p}} = \dot{\varepsilon}_r|\bar{\sigma}/g(\bar{\varepsilon}^{\mathrm{p}})|^{1/m}, \quad (10)$$

$$g(\bar{\varepsilon}^{\mathrm{p}}) = \sigma_r\{\tanh(k_1\bar{\varepsilon}^{\mathrm{p}}) + k_2 + H_e(\bar{\varepsilon}^{\mathrm{p}} - \varepsilon_r)k_3(\exp\bar{\varepsilon}^{\mathrm{p}} - \exp\varepsilon_r)\}, \quad (11)$$

where $g(\bar{\varepsilon}^{\mathrm{p}})$ is the flow stress model for PP, $\dot{\varepsilon}_r$ is the reference strain rate, σ_r is the reference stress, ε_r is the reference strain at which the second hardening begins. k_1–k_3 are material constants. $H_e(x)$ is the following step function.

$$H_e(x) = 1 \quad (\text{at } x > 0), \quad 0 \ (\text{at } x < 0). \quad (12)$$

The material properties of PP matrix were identified by the same authors in the previous study as shown in Table II.[41] SEBS particles were assumed to be elastic materials. Young's modulus and Poisson's ration were 1.4 MPa and 0.499.

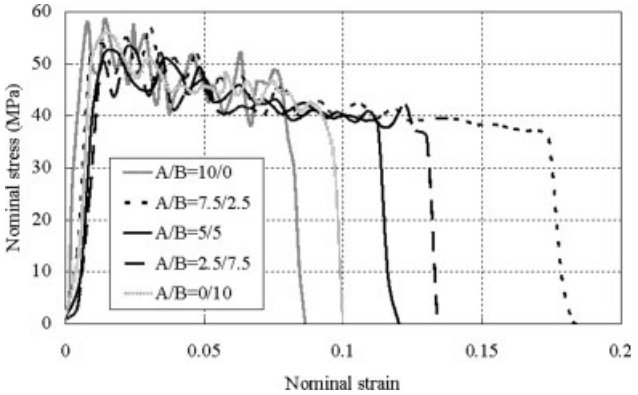

Figure 5 Typical stress strain curves of blend (PP/SEBS = 90/10) at the nominal strain rate of 100 s^{-1}.

In addition to the FE analyses for the blends of 90/5/5, 80/10/10 and 70/15/15, the morphological studies were analyzed by simply changing the meshes of SEBS A and B. In the FE models of the blends (80/10/10 and 70/15/15), a several FE meshes of SEBS A and B were got into the FE mesh of the PP matrix for changing the total area of SEBS A and B.

RESULTS AND DISCUSSION

Tensile mechanical properties of PP/SEBS blends

Tensile tests under each condition are conducted three times. The typical stress–strain curves of blends (PP/SEBS = 90/10 and 80/20) at the strain rate of 100 s^{-1} are shown in Figures 5 and 6. It is shown that the stress reduction of the blend (PP/SEBS A/SEBS B = 80/20/0 wt %) is the largest. On the contrary, the stress reduction was similar among all blends (PP/SEBS = 90/10 wt %), which indicates

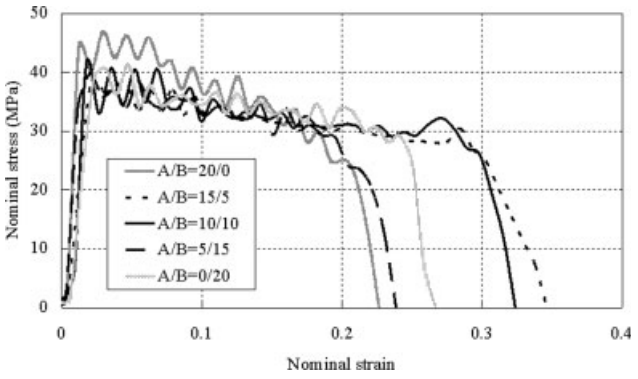

Figure 6 Typical stress–strain curves of blend (PP/SEBS = 80/20) at the nominal strain rate of 100 s^{-1}.

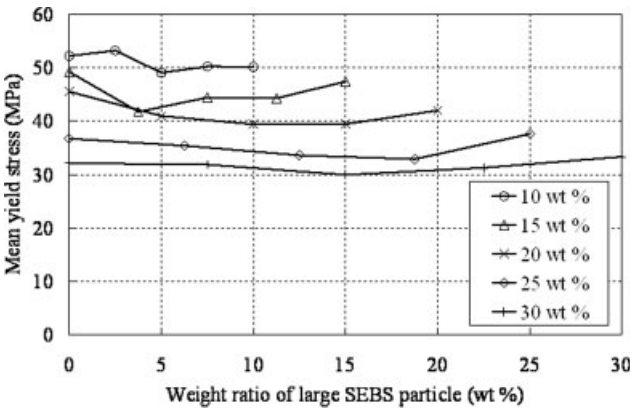

Figure 7 Mean yield stress of various blends at the nominal strain rate of 100 s^{-1}.

that the microdeformation mechanisms were similar among them. The following experimental results of the yield stress and the strain energy up to failure at the nominal strain rate of 100 s^{-1} are shown in this article. The experimental results at the nominal strain rates ranging from 0.3 to 50 s^{-1} can be found in the previous articles.[34,35] The yield stress was defined as the maximum nominal stress. The yield stress was measured three times at each condition, and then, the mean values are plotted in Figure 7. The yield stress showed the weak dependency of blend ratio at the nominal strain rate of 100 s^{-1}. The strain energy up to failure will be shown after the section of the fracture surface observation because the strain energy will be summarized with the various types of fracture mechanisms.

Fracture surfaces of PP/SEBS blends

The fracture surfaces of the blend (PP/SEBS = 85/15) at the nominal strain rate of 100 s^{-1} are shown in Figure 8. Figure 8 (a–c) shows the fracture surfaces of PP/SEBS A/SEBS B = 85/11.25/3.75, 85/7.5/7.5, and 85/3.75/11.25, respectively. In our previous study,[34] it is shown that the craze bands were main fracture mechanism in the blends (PP/SEBS A/SEBS B = 70/22.5/7.5 and 70/15/15 wt %). In this fracture mechanism, shear bands and crazes can be observed on the fracture surfaces. In the blend (PP/SEBS A/SEBS B = 70/7.5/22.5 wt %), the craze spot was the dominant fracture mechanism, leading to highly elongated fibril structures without large shear deformation of the matrix on the fracture surface. In Figure 8, the blends (PP/SEBS A/SEBS B = 85/7.5/7.5 and 85/3.75/11.25 wt %) show the similar fracture surface to those of blends (PP/SEBS A/SEBS B = 70/22.5/7.5 and 70/15/15 wt %). It is expected that the main fracture mechanism of the blends (PP/SEBS A/SEBS B = 85/7.5/7.5 and 85/3.75/11.25 wt %) could be craze bands. The validation for that is described in the estimation of interparticle distances.

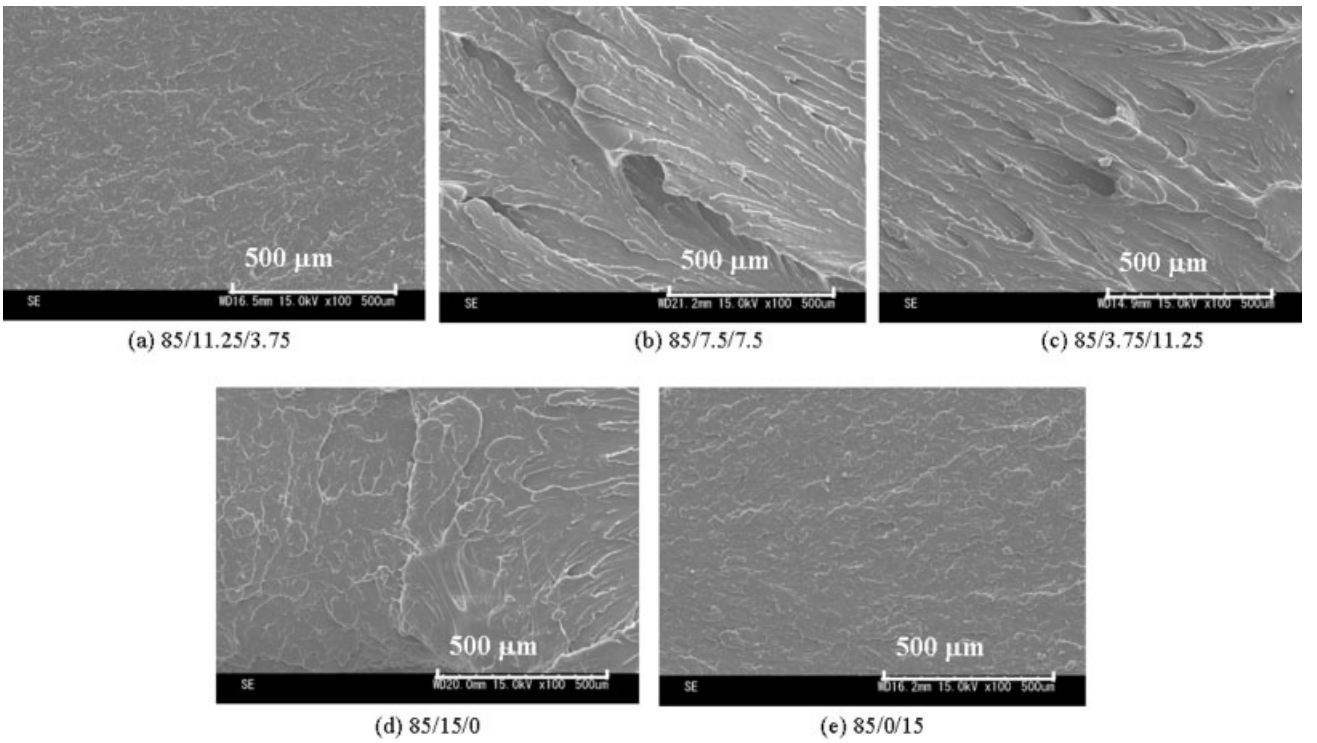

Figure 8 SEM pictures of fracture surfaces of the blends (PP/SEBS = 85/15).

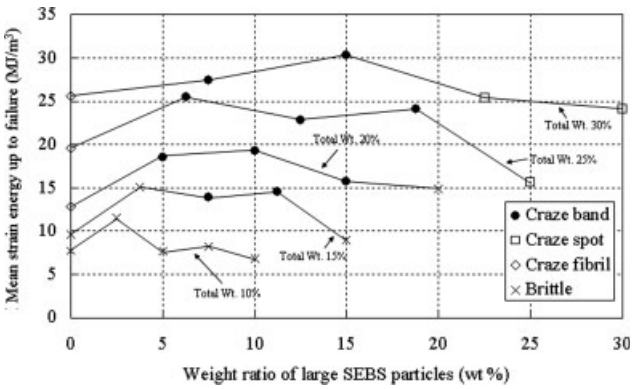

Figure 9 Strain energy up to failure of various blends at the nominal strain rate of 100 s^{-1}.

In other blends (PP/SEBS A/SEBS B = 90/7.5/2.5, 90/5/5, and 90/2.5/7.5 wt %), all the fracture surfaces were the brittle manner, which was completely different from those obtained in other blends. It is considered that the fracture mechanisms such as craze bands and craze spots do not occur in these blend systems.

As references, the fracture surfaces in monomodal SEBS blended PP (PP/SEBS = 85/15) at the nominal strain rate of 100 s^{-1} are shown in Figure 8(d,e). Both blends (PP/SEBS A/SEBS B = 85/15/0 and 85/0/15 wt %) show the brittle fracture surfaces, which is similar to Figure 8(a).

Based on these SEM observations of the fracture surfaces, the fracture types were identified in each blend. Finally, the strain energy up to failure is summarized in Figure 9. It is clear that the strain energy up to failure had the strong dependency of the blend ratio. As it is well known, the strain energy up to failure increased as the total rubber content increased. The interesting point here is that the strain energy up to failure reached to the maximum value in the blends where the weight ratio of large SEBS particles was about half of the total rubber content. In addition, it is noticeable that the craze band is the most effective fracture mechanism for increasing the strain energy up to failure.

Estimation of interparticle distances

It is well established that the interparticle distance between dispersed particles plays a crucial role to the mechanical properties, especially toughness, in polymer blends. Wu[36,42] proposed the concept of the critical ligament thickness that determines whether a blend will be tough or brittle. This concept has been applied to several rubber-toughened polymers, such as nylon,[36,42] PP,[43] and polyvinyl chloride.[44–49] For the cubic packing of spherical particles with uniform size, the matrix ligament thickness, i.e., interparticle distance (ID), can be obtained from eq. (13)

$$\mathrm{ID} = D\left[\left(\frac{\pi}{6\phi}\right)^{\frac{1}{3}} - 1\right], \tag{13}$$

where D is the rubber particle diameter, and ϕ is the rubber volume fraction. At the average particle diameter D, it is clear that ID decreases as the particle volume fraction increases. Based on the concept of stress concentration, the stress fields induced by both large and small particles can interact in all bimodal systems. It is well known that small particles cavitate and help to form the shear yielding of the matrix. The large particles are strongly related to craze formation.[35] Therefore, we focus on ID of large particles. Tables III shows the IDs of large particles calculated from eq. (13) in the blends (PP/SEBS = 70/30, 75/25, 80/20, 85/15, and 90/10 wt %), which are assumed that only large particles would be located in the matrix. Also, the IDs of large particles are directly measured from TEM images by image analyses in the blends (PP/SEBS A/SEBS B = 70/15/15, 80/10/10, and 90/5/5 wt %). The calculated results agree well with the results measured by TEM in the blends (PP/SEBS A/SEBS B = 70/15/15, 80/10/10, and 90/5/5 wt %). As the ratio of large particles increases, ID decreases and stress fields of each particle are overlapped. The stress interaction enhances the stress triaxiality, leading to craze formation easily.[35] In PP toughened by EOR, the critical ID ranges from 0.3 to 0.4 μm.[33] In the blend system

TABLE III
Estimated Interparticle Distances of Large SEBS Particles

SEBS A/SEBS B (wt %)	ID_{large} eq. (13) (nm)	ID_{large} image (nm)
10/0	–	–
7.5/2.5	438.38	–
5/5	296.49	320.54
2.5/7.5	227.47	–
0/10	183.85	–
15/0	–	–
11.25/3.75	351.43	–
7.5/7.5	227.47	–
3.75/11.25	167.16	–
0/15	129.05	–
20/0	–	–
15/5	296.49	–
10/10	183.85	219.64
5/15	129.05	–
0/20	94.43	–
25/0	–	–
18.75/6.75	257.35	–
12.5/12.5	152.78	–
6.25/18.75	101.91	–
0/25	69.76	–
30/0	–	–
22.5/7.5	227.47	188.6
15/15	129.05	133.3
7.5/22.5	81.18	89.4
0/30	50.93	–

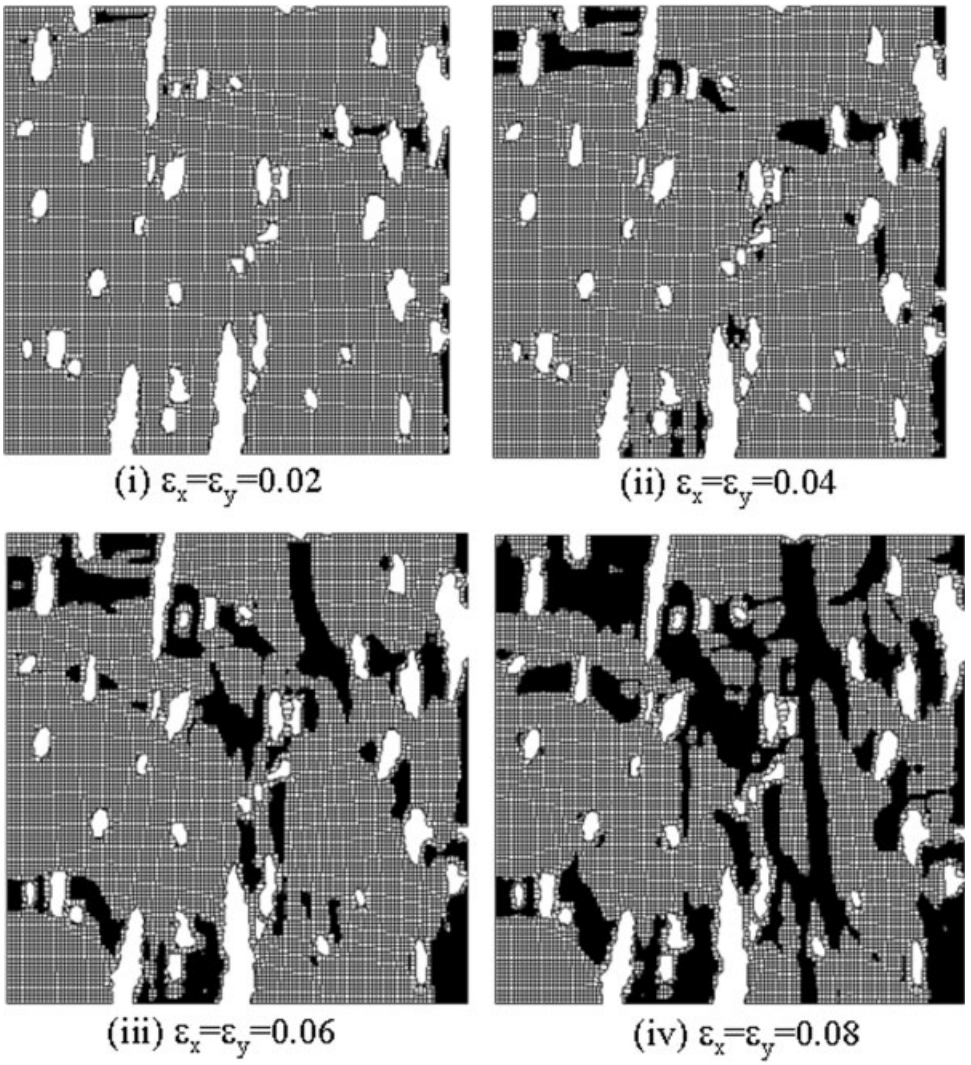

Figure 10 Snapshots of craze density of the blend 80/10/10. The black color region is the craze density larger than 0.9.

where the weight ratio of SEBS is 20 wt %, ID_{large} are less than 0.3 μm. Thus, it is considered that the stress interaction between large SEBS particles would occur in these blends. In the blends (PP/SEBS = 90/10 wt %), the interparticle distance larger than the critical ID was obtained in the blend (PP/SEBS A/SEBS B = 90/7.5/2.5 wt %). In this blend, it is considered that the stress interaction does not occur leading to the brittle fracture mechanism.

Results of numerical analyses

Figure 10 shows the craze density distribution in the case of 80/10/10. It is noted that all the SEBS particles are not shown in these figures for clear understanding of the craze density and stress distribution in PP matrix. As shown in Figure 10, the craze initiates at the boundaries between SEBS particles and PP matrix, and then grows in the perpendicular directions of the applied tensile directions and forms the network like craze bands. Finally, the craze grows up in most area of PP matrix. This craze growth so-called craze band is similar to the TEM morphological investigation obtained in the previous study.[34] Thus, it is considered that the simulated craze density can be used for investigating the ductility in various morphologies. The comparisons of the stress triaxiality and the craze density distribution at the nominal strain of 0.1 in x and y directions among three types of morphologies (90/5/5, 80/10/10, and 70/15/15) are shown in Figure 11. In Figure 11, the areas of the matrix where the stress triaxiality was larger than 2, and the craze density was above 0.9 are shown for a clearer understanding. The number shown below each figure indicates the large stress triaxiality and the high craze density areas divided by the area of PP matrix. The stress triaxiality per the unit area of PP matrix of the blend (90/5/5) was the largest among three blends while that of the high craze density was the smallest,

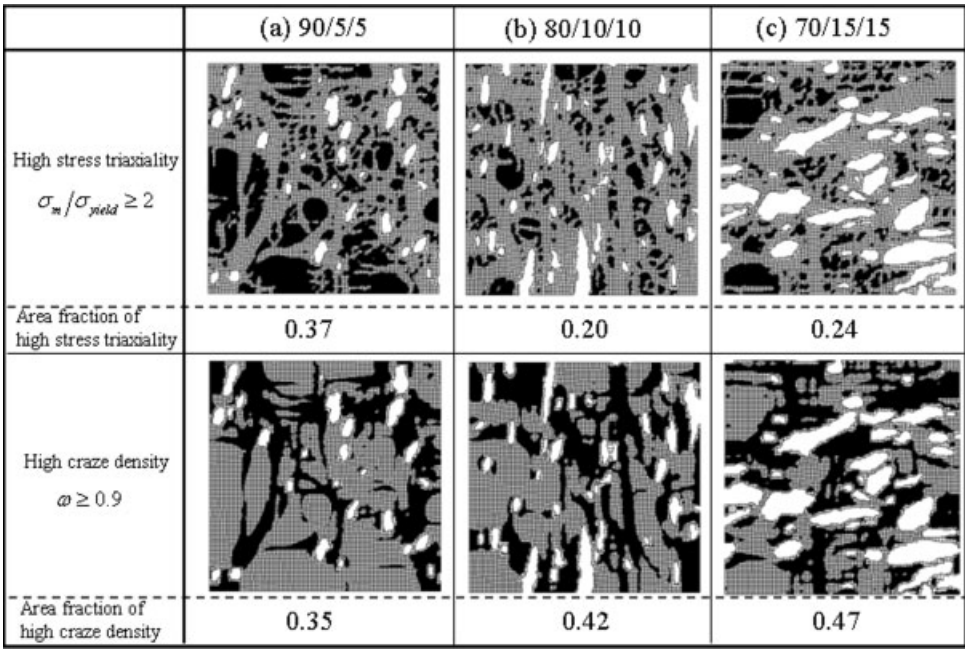

Figure 11 Distributions of high stress triaxiality and craze density of the blends (90/5/5, 80/10/10 and 70/15/15) at $\varepsilon_x = \varepsilon_y = 0.1$.

which meant that the blend (90/5/5) was the brittle fracture mechanism. This simulation result also agreed with the experimental observation. On the contrary, the stress triaxiality per unit area of PP matrix of the blend 70/15/15 was the smallest among three blends, whereas the craze density per unit area of PP matrix of the blend 70/15/15 was the largest among three blends. This numerical simulation was also good agreement with the experimental one. Based on the experimental observation, it is considered that the transition between the ductile and brittle fracture mechanisms would occur between 80/10/10 and 90/5/5. Then, the thresholds were interpolated between the simulation results of the blends (90/5/5 and 80/10/10) for simplicity, leading to the following two conditions for the ductile fracture mode. First, the fraction of the high-stress triaxiality should be smaller than 0.285 for the ductile fracture mechanism. Second, the fraction of the high-craze density should be larger than 0.385. It is clear that the blend of the small total rubber contents showed the large area of the high-stress triaxiality, leading to the brittle fracture. On the contrary, the blend which consisted of the large total rubber content such as the blend 70/15/15 showed the large area of the high-craze density leading to the ductile fracture mode. Then, the additional FE analysis was conducted for investigating the ductile brittle transition by changing the areas of SEBS A and B in the FE models of the blends (80/10/10 and 70/15/15). Figure 12 shows the distributions of the high-stress triaxiality and the large craze density at $\varepsilon_x = \varepsilon_y = 0.1$ in the morphological models where the volume fraction of SEBS A was changed in the base model of the blend (80/10/10). It is considered that the ductile brittle transition could occur between the blends of 85/5/10 and 87.5/2.5/10 based on the afore-mentioned thresholds. In the same manner, it is expected the ductile brittle transition would occur at the blends between 82.5/10/7.5 and 85/10/5 as shown in Figure 13. The same morphological FE analysis was conducted on the blend model of 70/15/15. The results showed that the ductile brittle transition was found in the blends between 83.1/1.9/15 and 85/0/15 where the blend ratio of SEBS B was fixed as 15 wt % while that was found in the blends between 81.2/15/3.8 and 83.1/15/1.9. Based on these numerical simulation results in addition to the experimental results, the material ductility and toughening mechanisms are summarized in the following section.

Summary of material ductility and toughening mechanisms

For summarizing the toughening mechanisms, it is necessary to consider the location of small SEBS particles in PP matrix in addition to the estimated ID_{large}. Because small SEBS particles are well dispersed as already shown in Figure 2, the location of small SEBS particles is considered as the weight ratio of small SEBS particles against the total SEBS particles in this study. Figure 14 shows the relationship between the weight ratio of small SEBS particle against total SEBS particles and the interparticle

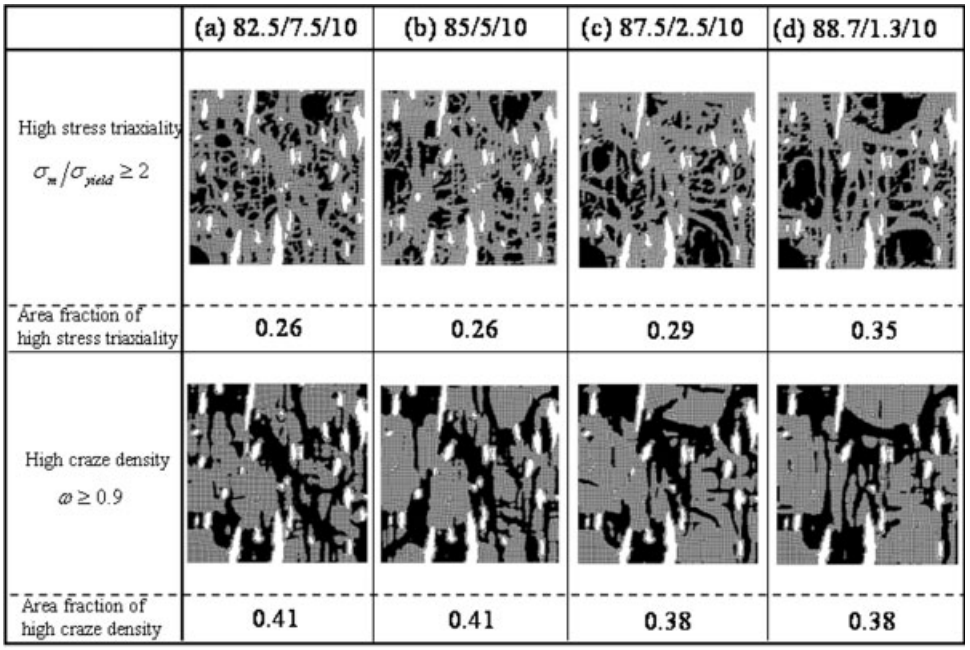

Figure 12 Comparisons of high-stress triaxiality and craze density at $\varepsilon_x = \varepsilon_y = 0.1$ in the various SEBS A contents.

distance of large SEBS particles where the results of the morphological studies obtained in the FE models are plotted in addition to the experimental results. As shown in Figure 14, the clear thresholds are observed among various fracture modes. It is expected that the inter particle distance of large SEBS particles should be larger than 100 nm for making rooms between the large SEBS particles for the small SEBS particles. As the interparticle distance of the large SEBS particles increases, the necessary volume ratio of small SEBS particles against the large SEBS particles should get larger for keeping the material ductility, leading to the gradual increase of the thresholds of the small SEBS particles. Figure 15 shows the relationship between the weight ratio of small SEBS and that of large SEBS particles with fracture mechanisms with the results of the morphological studies obtained by the FE models. Here, this study focused on the total rubber content smaller than 30 wt % because the total rubber content is

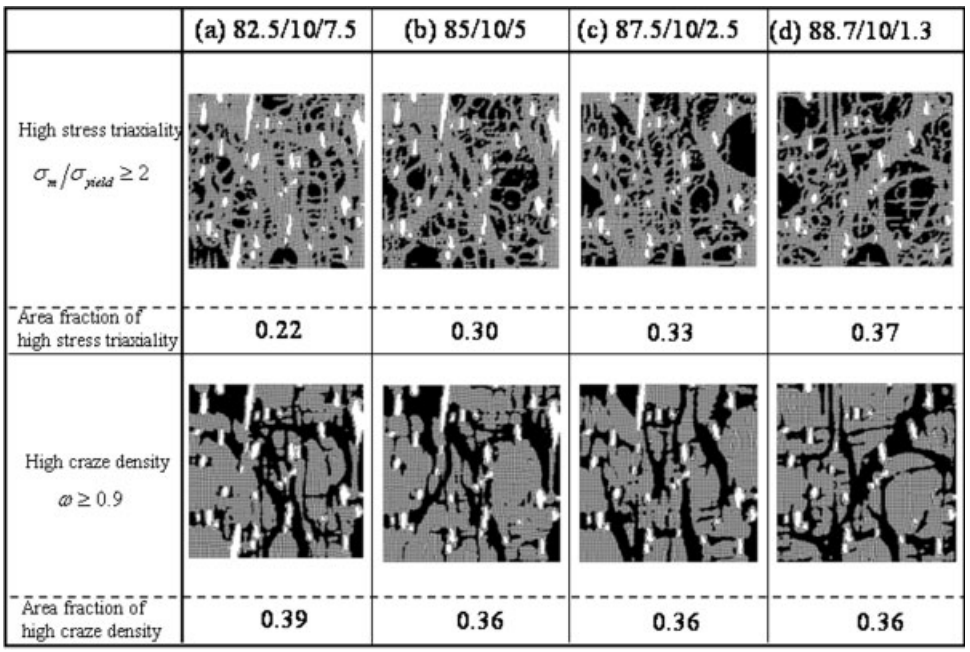

Figure 13 Comparisons of high-stress triaxiality and craze density at $\varepsilon_x = \varepsilon_y = 0.1$ in the various SEBS B contents.

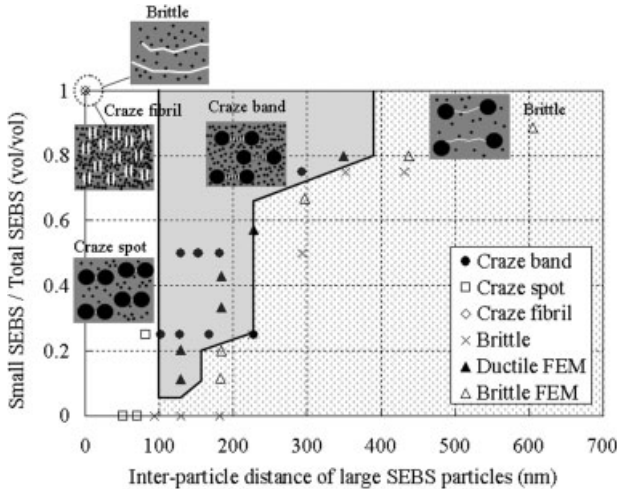

Figure 14 Weight ratio of small SEBS against total SEBS content versus interparticle distance of large SEBS particles with toughening models of bimodal particle blends.

smaller than 30 wt % from the practical application point of view. As shown clearly, the craze bands were obtained at the total weight ratio of SEBS particles larger than 15 wt %. In the present blend system, it is considered that the key conditions for craze bands should be three points. First, the total SEBS content should be larger than 15 wt %. Second, the interparticle distance of large SEBS particles should be larger than 100 nm. Third, the volume ratio of small SEBS particle against total SEBS particles should be larger than 0.06, leading to locate small SEBS particles between large SEBS particles.

Therefore, the total rubber content, the interparticle distance of large particles and the location of small particles are the key factors for improving the ductility of the bimodal polymer blends where the total rubber content ranges from 10 to 30 wt %.

CONCLUSIONS

The material ductility and toughening mechanisms under high-strain rate are characterized in the PP blended with two different SEBS particles. It is found that the bimodal distributed SEBS particle morphology enhances the impact material ductility by the toughening mechanism of craze bands. These toughening mechanisms are described by the tensile tests at the nominal strain rates from 0.3 to 100 s^{-1}, fracture surface observations, interparticle distances, and the morphological FE analyses. The microstructural FE analysis was also conducted by using the elasto–visco–plastic constitutive law with craze nucleation and growth. The followings are the conclusions of this study:

1. The yield stress has the weak morphological dependency of bimodally distributed particle size at the high strain rate.
2. The absorbed strain energy has strong dependency of bimodally distributed rubber particle size in the morphology in the blends (PP/SEBS = 70/30, 75/25, 80/20, and 85/15 wt %). On the contrary, the blend (PP/SEBS = 90/10 wt %) shows different trend of the ductility.
3. The large material ductility is obtained in the fracture mechanism of craze bands. The craze bands are caused by the stress interaction between large rubber particles with the highly elongated small rubber particles inside the fibrils of the craze. The craze bands occur in the blend where the total SEBS content is larger than 15 wt %. In addition, the condition for craze bands is that the weight ratio of small SEBS particles against total SEBS particles should be larger than 0.06 and the interparticle distance of large SEBS particles should be larger than 100 nm. This result validates the result of our previous study where the important parameters for toughening are the location of the small particles and the distance of large particles.
4. The elasto–visco–plastic constitutive law with craze nucleation and growth could simulate successfully the microstructural craze-band nucleation and growth.
5. The ductile brittle transition could be identified by combining the experimental and numerical approaches in the microstructural-scale FE models.

Based on the results of this study, it is expected that the more precisely distributed bimodal rubber particle blend system could decrease the total rubber content while the material is kept more ductile even at the impact loading condition.

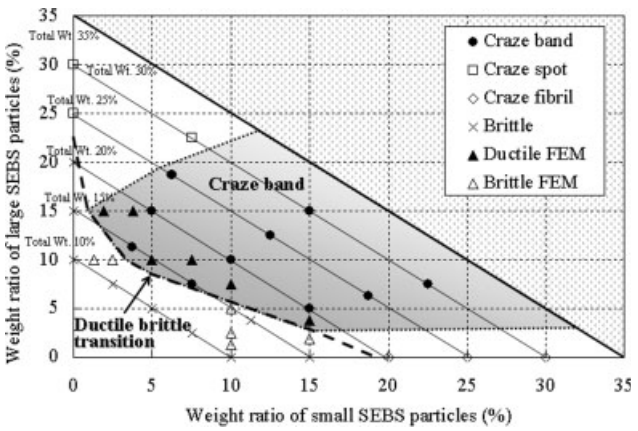

Figure 15 Weight ratio of small SEBS versus weight ratio of large SEBS particles.

The authors would like to acknowledge Centre for Advanced Materials Analysis, Tokyo Institute of Technology, for helping the TEM observation.

References

1. Mae, H.; Takada, K.; Takahashi, J.; Yamamoto, T. Honda R&D Tech Rev 2004, 16, 165.
2. Mae, H.; Omiya, M.; Kishimoto, K. Mater Sci Eng A 2008, 477, 168.
3. Mae, H.; Omiya, M.; Kishimoto, K. J Solid Mech Mater Eng 2008, 2, 616.
4. William, G. P.; Polym Eng Sci 1999, 39, 2445.
5. D'Orazio, L.; Mancarella, C.; Martuscelli, E.; Polato, F. Polymer 1991, 32, 1186.
6. Stehling, F. C.; Huff, T.; Speed, C. S.; Wissler, G. J Appl Polym Sci 1981, 26, 2693.
7. Karger-kocsis, J.; Kallo, A.; Kuleznev, V. N. Polymer 1984, 25, 279.
8. Van der Waal, A.; Nijhof, R.; Gaymans, R. J Polymer 1999, 40, 6031.
9. Moore, E. P. Polypropylene Handbook; Hanser Verlag: Munchen, 1996.
10. Liu, Y. Q.; Kontopoulou, M. Polymer 2006, 47, 7731.
11. Qiu, G. X.; Zhang, P.; Pan, J. X.; Zhao, S. G. Polym-Plastic Tech Eng 2003, 42, 33.
12. Liang, J. Z., Li, R. K. Y. J Appl Polym Sci 2000, 77, 409.
13. Jang, B. Z.; Uhlmann, D. R.; Vander Sande, J. B. Polym Eng Sci 1985, 25, 643.
14. Jang, B. Z.; Uhlmann, D. R.; Vander Sande, J. B. J. Appl Polym Sci 1985, 30, 2485.
15. Margolina, A.; Wu, S. Polymer 1988, 29, 2170.
16. Holz, N.; Goizueta, G. S.; Capiati, N. J Polym Eng Sci 1996, 36, 2765.
17. Ou, Y. C.; Guo, T. T.; Fang, X. P.; Yu, Z. Z. J Appl Polym Sci 1999, 74, 2397.
18. Molnar, S.; Pukanszky, B.; Hammer, C. O.; Maurer, F. H. J. Polymer 2000, 41, 1529.
19. Lim, J. W.; Hassan, A.; Rahmat, A. R.; Wahit, M. U. Plastic Rub Comp 2006, 35, 37.
20. Borggreve, R. J. M.; Gaymans, R. J.; Schuijer, J.; Ingen Housz, J. F. Polymer 1987, 28 1489.
21. Speri, W. M.; Patrick, G. R. Polym Eng Sci 1975, 15, 668.
22. Dao, K. C. Polymer 1984, 25, 1527.
23. Horiuchi, S.; Matchariyakul, N.; Yase, K.; Kitano, T.; Choi, H. K.; Lee, Y. M. Polymer 1997, 38, 59.
24. Jar, P.-Y.; Lee, R.; Shinmura, T.; Konishi, K. J Polym Sci Part B: Polym Phys 1999, 37, 1739.
25. Cho, K.; Yang, J. H.; Yoon, S.; Nair, M. J Appl Polym Sci 2005, 95, 748.
26. Van der Waal, A.; Verheul, A. J.; Gaymans, R. J Polymer 1999, 40, 6057.
27. Stricker, F.; Thomann, Y.; Mulhaupt, R. J Appl Polym Sci 1998, 68, 1891.
28. Mae, H.; Omiya, M.; Kishimoto, K. J Solid Mech Mater Eng 2008, 2, 254.
29. Chen, T. K.; Jan, Y. H. J Mater Sci 1992, 27, 111.
30. Fowler, M. E.; Keskkula, H.; Paul, D. R. J Appl Polym Sci 1987, 28, 2145.
31. Fowler, M. E.; Keskkula, H.; Paul, D. R. J Appl Polym Sci 1988, 35, 1563.
32. Premphet, K.; Paecharoenchai, W. J Appl Polym Sci 2001, 82, 2140.
33. Premphet, K.; Paecharoenchai, W. J Appl Polym Sci 2002, 85, 2412.
34. Mae, H.; Omiya, M.; Kishimoto, K. J Appl Polym Sci 2008, 107, 3520.
35. Mae, H.; Omiya, M.; Kishimoto, K. J Soc Mater Sci Japan 2008, 57, 951.
36. Wu, S. Polymer 1985, 26, 1855.
37. Finite Element Analysis of Microstructures, Available at: http://www.ctcms.nist.gov/oof/
38. Murakami, D.; Kobayashi, S.; Torigaki, T; Shizawa, K. Trans Jpn Soc Mech Eng A 2002, 68, 674.
39. Murakami, D.; Kobayashi, S.; Torigaki, T.; Shizawa, K. Trans Jpn Soc Mech Eng A 2002, 68, 682.
40. Kobayashi, S.; Tomii, D.; Shizawa, K. Trans Jpn Soc of Mech Eng A 2004, 70, 810.
41. Mae, H.; Omiya, M.; Kishimoto, K. J Solid Mech Mater Eng 2007, 1, 35.
42. Wu, S. J Appl Polym Sci 1988, 35, 549.
43. Jancar, J.; Dianselmo, A.; Dibenedetto, A. T. Polym Commun 1991, 32, 367.
44. Liu, Z. H.; Zhang, X. D.; Zhou, X. G.; Qi, Z. N.; Wang, F. S. Polymer 1997, 21, 5267.
45. Liu, Z. H.; Li, R. K. Y.; Tjong, S. C.; Qi, Z. N.; Wang, F. S.; Choy, C. L. Polymer 1998, 39, 4433.
46. Liu, Z. H.; Zhang, X. D.; Zhu, X. G.; Li, R. K. Y.; Qi, Z. N.; Wang, F. S.; Choy, C. L. Polymer 1998, 39, 5019.
47. Liu Z. H.; Zhang, X. D., Zhu, X. G.; Qi, Z. N.; Wang, F. S.; Li, R. K. Y.; Choy, C. L. Polymer 1998, 39, 5027.
48. Liu Z. H.; Zhang, X. D.; Zhu, X. G.; Li, R. K. Y.; Qi, Z. N.; Wang, F. S.; Choy, C. L. Polymer 1998, 39, 5031.
49. Liu Z. H.; Zhang, X. D.; Zhu, X. G.; Qi, Z. N.; Wang, F. S.; Li, R. K. Y.; Choy, C. L. Polymer 1998, 39, 5047.